

Current sheet bending as destabilizing factor in magnetotail dynamics

D. B. Korovinskiy, V. S. Semenov, N. V. Erkaev, I. B. Ivanov, and S. A. Kiehas

Citation: [Physics of Plasmas](#) **25**, 092901 (2018); doi: 10.1063/1.5046175

View online: <https://doi.org/10.1063/1.5046175>

View Table of Contents: <http://aip.scitation.org/toc/php/25/9>

Published by the [American Institute of Physics](#)

PHYSICS TODAY

WHITEPAPERS

MANAGER'S GUIDE

Accelerate R&D with
Multiphysics Simulation

READ NOW

PRESENTED BY

 **COMSOL**

Current sheet bending as destabilizing factor in magnetotail dynamics

D. B. Korovinskiy,^{1(a)} V. S. Semenov,² N. V. Erkaev,^{2,3,4} I. B. Ivanov,⁵ and S. A. Kiehas¹

¹Space Research Institute, Austrian Academy of Sciences, 8042 Graz, Austria

²The Earth Physics Department, Saint Petersburg State University, 198504 Petrodvorets, Russia

³Institute of Computational Modelling, Siberian Branch, Russian Academy of Sciences, 660036 Krasnoyarsk, Russia

⁴The Applied Mechanics Department, Siberian Federal University, 660041 Krasnoyarsk, Russia

⁵Theoretical Physics Division, Petersburg Nuclear Physics Institute, 188300 Gatchina, Russia

(Received 26 June 2018; accepted 21 August 2018; published online 7 September 2018)

The problem of the magnetohydrodynamical stability of bent magnetotail current sheets is considered by means of 2.5-dimensional numerical simulations. This study is focused on the cross-tail transversal mode, modeling the magnetotail flapping motions, at the background of the Kan-like magnetoplasma equilibrium. It is found that in symmetrical current sheets, both stable and unstable branches of the solution may coexist; the growth rate of the unstable mode is rather small, so that the sheet may be considered as stable at the substorm timescale. With the increasing dipole tilt angle, the sheet bends and the growth rate rises. For sufficiently large tilt angles, the stable branch of the solution disappears. Thereby, the sheet destabilization timescale shortens for an order of magnitude, down to several minutes. The analysis of the background parameters has shown that stability loss is not related to buoyancy; it is controlled by the cross-sheet distribution of the total pressure. © 2018 Author(s). All article content, except where otherwise noted, is licensed under a Creative Commons Attribution (CC BY) license (<http://creativecommons.org/licenses/by/4.0/>). <https://doi.org/10.1063/1.5046175>

I. INTRODUCTION

According to the hypothesis of Kivelson and Hughes,¹ the threshold of the instability, responsible for the onset of magnetospheric substorms, should decrease with the increasing magnetic dipole tilt since bending of the magnetotail current sheet (CS) is to be accompanied by an enhancement of the magnetic field gradients and current density. This hypothesis has found some confirmation in observational data analysis: breaking of the CS symmetry due to the dipole inclination and variations of solar wind velocity component V_z and interplanetary magnetic field B_x are found to decrease the substorm threshold and increase the substorm occurrence rate for 10%–25%;^{2–4} for influence on the CS stability, see also Refs. 5 and 6.

The physical mechanism of substorm onset stays in focus of scientific studies for decades and is still debated. However, it is well known that this explosive magnetotail process is often accompanied by magnetic reconnection, flapping motions, and ballooning/interchange (BICI) instability (see, e.g., Ref. 7 and references therein). This allows the assumption that the stability/instability of the magnetotail CS to these modes may be interrelated to a substorm expectancy. Studies of the BICI mode reveal that it is controlled by the distribution of the normal magnetic component B_z in the CS center: local humps of B_z make the sheet unstable (e.g., Refs. 8 and 9). This behavior may also be treated in terms of the entropy criterion:¹⁰ the sheet is stable when the entropy monotonically increases tailward.

The flapping mode is usually observed as kink-like perturbations, propagating across the magnetotail CS in dawn and dusk directions. Since the first detection by Ness,¹¹ these

motions have been registered many times in the magnetospheres of Earth,^{12–19} Venus,^{20–22} Jupiter, and Saturn.^{23–25} Our previous study has confirmed that local peaks of B_z make the CS unstable to the flapping mode.²⁶ But is that the only mechanism of the mode destabilization in magnetohydrodynamical (MHD) approximation?

The present study is motivated by two recent findings. In Ref. 27, the stability of the symmetrical CS to the flapping mode was examined. It was found that the cross-sheet profile of the total (gas+magnetic) pressure controls the sheet stability: CS is stable when the total pressure reaches a minimum in the center and vice versa. In Ref. 28, we examined a Kan-like analytical model of bent current sheets. It was found that (a) the model shows good agreement with the model of Tsyganenko²⁹ for any level of magnetospheric activity, i.e., the model is more or less realistic, and (b) CS bending does not produce any crucial changes in the main characteristics of the current layer, such as current density and entropy. This means that according to the entropy criterion, the stability of the Kan-like CS should not depend on its bending.

In the current paper, we present a numerical investigation of the bent CS stability to the flapping mode, aiming to answer two questions: (a) is the entropy criterion appropriate for the flapping mode? and (b) how does CS bending modify the total pressure distribution and how does it affect the CS stability? This paper is organized as follows: in Sec. II, we describe the analytical solution for bent equilibrium current sheets; in Sec. III, we outline the numerical technique; in Sec. IV, we outline the double-gradient (DG) model,³⁰ used as the analytical bench mark; the results are presented in Sec. V; and discussion and conclusions finalize the paper in Sec. VI.

^{a)}Electronic mail: daniil.korovinskiy@oeaw.ac.at

II. BACKGROUND EQUILIBRIUM

As a background magnetoplasma configuration, we utilize the generalized 2D Kan-like kinetic solution²⁸ of the Vlasov-Maxwell equations, derived from the solution of Yoon and Lui³¹ after introducing complex parameters.³² In a reference system, where the x axis points tailward, the y axis points downward, and the z axis points north, the solution for the dimensionless magnetic potential $\Psi(x, z)$ takes the form

$$\Psi = \ln \left(\frac{f \cos X_* + \sqrt{1+f^2} \cosh Z_*}{\sqrt{W}} \right), \quad (1)$$

$$X_* = r^n \cos(n\vartheta) - \frac{b_0}{R^k} \cos(k\Theta - \varphi), \quad (2)$$

$$Z_* = r^n \sin(n\vartheta) + \frac{b_0}{R^k} \sin(k\Theta - \varphi), \quad (3)$$

$$W = n^2 r^{2(n-1)} + \frac{b_0^2 k^2}{R^{2(k+1)}} + 2nk b_0 \frac{r^{n-1}}{R^{k+1}} \cos[(n-1)\vartheta + (k+1)\Theta - \varphi], \quad (4)$$

$$r = \sqrt{x^2 + z^2}, \quad \vartheta = \arctan\left(\frac{z}{x}\right), \quad (5)$$

$$R = \sqrt{(x-a_1)^2 + (z-a_2)^2}, \quad \Theta = \arctan\left(\frac{z-a_2}{x-a_1}\right), \quad (6)$$

where real values $\{a_1, a_2, b_0, \varphi, f, k, n\}$ are the dimensionless model parameters. Parameters a_1 and a_2 control the shift in horizontal and vertical directions, respectively; parameter b_0 controls the field line stretching; φ scales the dipole tilt angle; f defines the current density in the magnetic islands; parameter k contributes the field line elongation and dipole tilt; and n controls the field line flaring. Then, expressions for magnetoplasma quantities are

$$B_x = -\frac{\partial \Psi}{\partial z}, \quad B_y = 0, \quad B_z = +\frac{\partial \Psi}{\partial x}, \quad (7)$$

$$\rho = \exp(-2\Psi) + \rho_b, \quad p = 0.5 \exp(-2\Psi). \quad (8)$$

Here, ρ is the mass density, ρ_b is the mass density of the additional cold plasma component (required to reduce the Alfvén velocity in numerical simulations), p is the plasma pressure, and plasma velocity \mathbf{V} and electric potential ϕ are zero. The set of normalization constants includes the sheet typical half-width L , the lobe magnetic field B_0 , the typical mass density ρ_0 , the Alfvén velocity $V_a = B_0/\sqrt{4\pi\rho_0}$, and the pressure $p_0 = B_0^2/(4\pi)$. Though isothermal, this model is found to be appropriate for modeling of not too thin ($L \gtrsim 0.5 R_E$) current sheets.²⁸ In such sheets, normalization parameters attain reasonable values and the distribution of the magnetic flux tube volume shows good agreement with the T96 model²⁹ for all levels of magnetospheric activity.

III. NUMERICAL SIMULATIONS

In this section, we present a brief outline of the applied numerical technique; a detailed description is provided in Ref. 33. Our study is focused on transversal perturbations,

propagating in equilibrium media. A system of 3D ideal compressible MHD equations³⁴ is linearized, and the solution $\sim \exp(ik_y y)$, where k_y is the wave number, is sought for. Hence, the problem is reduced to a 2.5-dimensional system of equations for perturbation amplitudes, stated in conservative form

$$\frac{\partial(\delta \mathbf{U})}{\partial t} + \frac{\partial \mathbf{F}_x}{\partial x} + \frac{\partial \mathbf{F}_z}{\partial z} = \mathbf{S}, \quad (9)$$

where

$$\delta \mathbf{U}(x, z, t; k_y) = (\delta \rho, \{\delta M_i\}, \{\delta B_i\}, \delta E)_{i=x,y,z}. \quad (10)$$

Here, $\delta \mathbf{U}$ stands for the 8-component complex vector of perturbation amplitudes, $M_i = \rho V_i$ are the momentum components, $E = p/(\kappa - 1) + 0.5\rho V^2 + 0.5B^2$ is the total energy density, and $\kappa = 5/3$ is the polytropic index. Expressions for flux densities \mathbf{F}_x and \mathbf{F}_z and the source term \mathbf{S} , depending on x, z, k_y , and initial state \mathbf{U}_0 , are given in the Appendix of Ref. 33. Normalization is the same as in Sec. II, with the time scale $t_0 = L/V_a$. Equation (9) is solved numerically by means of the 3rd order central semi-discrete upwind scheme³⁵ with open boundary conditions $\partial/\partial \mathbf{n} = 0$. We have used the strong stability preserving Runge-Kutta method of the 3rd order.³⁶ The integration time step (Courant–Friedrichs–Lewy number 0.5) is adopted to ensure the convergence of the results with respect to the values of the time step. The $\nabla \cdot \mathbf{B} = 0$ constraint is enforced on each time step by using the method of projection.³⁷ Additionally, at each time step, three components of the displacement vector ξ are computed. Simulations are seeded with the initial perturbation of the normal velocity component, $v_z|_{t=0} = \exp(-z^2)$. Since the initial perturbation is real, the vector $\delta \mathbf{U}$ has only eight non-zero components: $\Re(\delta \rho)$, $\Re(\delta M_x)$, $\Im(\delta M_y)$, $\Re(\delta M_z)$, $\Re(\delta B_x)$, $\Im(\delta B_y)$, $\Re(\delta B_z)$, $\Re(\delta E)$.

IV. ANALYTICAL MODEL

The results of our previous simulations for symmetric planar current sheets have shown good agreement^{27,33} with the predictions of the so-called double-gradient (DG) model of flapping oscillations.^{30,38} Therefore, the results of the present numerical studies are also compared to them. The DG model utilizes the quasi-one-dimensional approach, based on a number of simplifying assumptions: (a) the CS is stretched, so that $\nu = L/L_x \ll 1$, where L_x is the typical sheet length; (b) the normal magnetic component is small, so that $\epsilon = \max(B_z)/\max(B_x) \ll 1$; and (c) $\epsilon/\nu \ll 1$. Under these assumptions, the terms $\sim \nu^2 \epsilon$ and $\sim \epsilon^2$ are neglected [see underlined terms of Eq. (10) in Ref. 30], and system (9) is reduced to a single equation for v_z

$$\frac{1}{\rho} \frac{d}{dz} \left(\rho \frac{dv_z}{dz} \right) + k_y^2 v_z \left(\frac{U_0}{\omega^2} - 1 \right) = 0, \quad (11)$$

$$U_0 = \frac{1}{\rho} \frac{\partial B_x}{\partial z} \frac{\partial B_z}{\partial x}. \quad (12)$$

Here, U_0 , ρ , and v_z are assumed to be dependent on the z coordinate only, and ω is the angular frequency of the

perturbations $\sim \exp[i(k_y y - \omega t)]$. In planar CS, Eq. (11) allows two independent branches of the solution:³⁰ an infinite set of kink-like modes (v_z is an even function of z) and an infinite set of sausage-like modes (v_z is odd). In a bent CS, the symmetry is destroyed; hence, both modes are coexistent and the solution may be represented as a combination $v_z = c_1 v_z^{\text{even}} + c_2 v_z^{\text{odd}}$. Coefficients $c_{1,2}$ are not independent; however, they may be chosen to provide $v_z^{\text{even}}(0) = v_z^{\text{odd}}(0) = 1$, where prime stands for d/dz . Dividing the solution by $\sqrt{c_1^2 + c_2^2}$, we can write $v_z = \cos(\alpha) v_z^{\text{even}} + \sin(\alpha) v_z^{\text{odd}}$. Then, the spectral problem is set by complementing Eq. (11) with the boundary conditions

$$v_z(0) = \cos(\alpha), \quad \frac{dv_z}{dz}(0) = \sin(\alpha), \quad (13)$$

$$\frac{dv_z}{dz}(+z_b) = -k_y v_z(+z_b), \quad \frac{dv_z}{dz}(-z_b) = +k_y v_z(-z_b). \quad (14)$$

Conditions (13) specify the solution in the point $z = 0$; conditions (14), where z_b is the upper z -boundary as a proxy of infinity, assume v_z to decrease exponentially outside the CS, $v_z \rightarrow \text{const} \cdot \exp(-k_y |z|)$. The unknown eigenfrequency and parameter α are determined by matching the solutions obtained in upper, $z \in [0, z_b]$, and lower, $z \in [-z_b, 0]$, semiplanes.

It is noteworthy that if function $U_0(z)$ is of a constant sign, the solution of the problem [(11)–(14)] has the form of a pure oscillating mode ($U_0 > 0$) or a pure unstable mode ($U_0 < 0$) since $\text{sign}(\omega^2) = \text{sign}(U_0)$. For alternating-sign functions U_0 , the DG model has not been tested for now.

V. RESULTS

To examine the influence of a magnetic dipole tilt on the CS stability to the transversal mode, we consider a set of five background configurations (1–8), where parameters $\{a_1 = 0, a_2 = 0, b_0 = 9, f = 0, k = 0.5, \text{ and } n = 1\}$ are the same, and parameter φ takes values of $\{0^\circ, 7.5^\circ, 15^\circ, 30^\circ, 60^\circ\}$ clockwise. When parameter $k = 1$, the dipole tilt angle scales²⁸ as $\varphi/2$; in our case, the scale factor is $2/3$. Hence, the value $\varphi = 60^\circ$ corresponds approximately to the maximum effective dipole tilt for terrestrial conditions (dipole inclination for 33° plus 8° deviation of the solar wind velocity from the horizontal direction; see Ref. 3). The set of other parameters corresponds to the quiet magnetotail [see Fig. 4(a) in Ref. 28]. The mass density of the cold plasma population $\rho_b = 0.1$ is the same for all runs. Magnetic configurations for $\varphi = \{0^\circ, 15^\circ, 30^\circ, 60^\circ\}$ are exhibited in Fig. 1, where magnetic field lines are plotted by the contour curves of Ψ , shown by color, and white curves mark the sheet centers, defined as the loci of peaking current density.

Equation (9) is solved numerically for a set of dimensionless wavenumbers $k_y = \{1/4, 1/2, 1, 4/3, 2, 4\}\pi$. In dimensional units, it corresponds to wavelengths $\lambda = \{8, 4, 2, 3/2, 1, 1/2\}L$. Simulations are run in a symmetrical box $x \in [14, 16]$ and $z \in [-z_b, +z_b]$ with $dx = dz = 1/2^5$. Cross-sheet profiles of eigenfunctions thin³³ with increasing k_y , and hence, the value of z_b varies from 70 to 20. The small value of the box length is chosen to save computational time; this

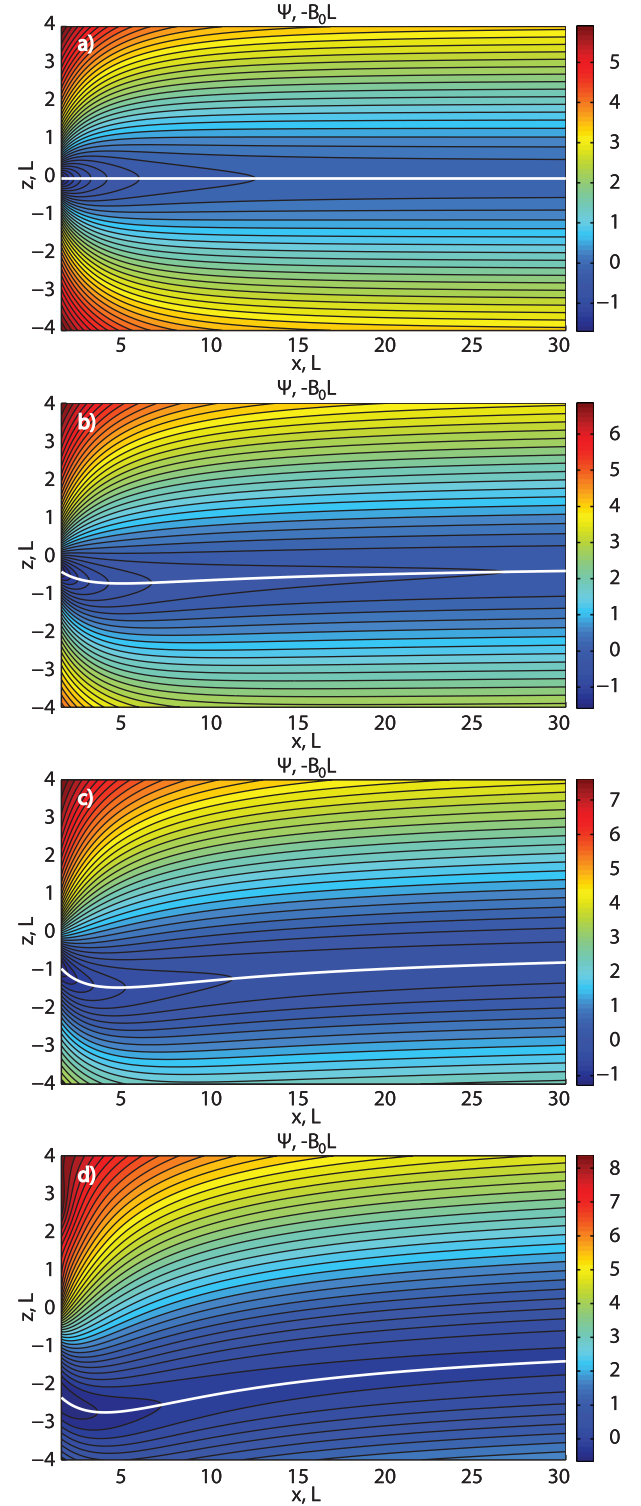


FIG. 1. Four magnetic configurations, calculated from Eqs. (1)–(6) with $\varphi = \{0^\circ, 15^\circ, 30^\circ, 60^\circ\}$ clockwise, are shown on panels (a)–(d), respectively. Other parameters are the same: $a_1 = a_2 = f = 0$, $b_0 = 9$, $k = 0.5$, and $n = 1$. The value of the normalized magnetic potential Ψ is shown by color, magnetic field lines are plotted by contour curves, and white curves depict the CS centers. The dipole tilt angle scales as $2\varphi/3$.

is enabled by the slow variation of the CS parameters in the x direction. Indeed, control simulations in a wider box $x \in [10, 20]$ have shown a negligible difference in results.

The sample solution $\ln|\delta U|(t)$ in the point $(x, z) = (15, 0)$ for $\lambda = L$ and $\varphi = 0^\circ$ is shown in Fig. 2(a) by thin curves.

Thick curves show the solutions for momentum component δM_z for $\varphi = \{0^\circ, 7.5^\circ, 15^\circ, 30^\circ, 60^\circ\}$. In symmetrical CS, we observe the coexistence of oscillating and unstable modes, where the first one may be detected up to $t \approx 700$, and the second one is not manifested until $t \approx 500$. For $\varphi = 7.5^\circ$, the unstable regime is also settled after $t = 700$. For $\varphi = 15^\circ$, the oscillating mode survives up to $t \approx 500$ (manifested in the solution for δB_z , not shown) and unstable one comes in sight at $t \approx 200$. For $\varphi = 30^\circ$ and 60° , the oscillating mode is barely detectable, and exponential growth dominates from $t \approx 100$ and less. Thus, the stability of the CS to the transversal mode drops down with the sheet bending.

The interplay of the stable and unstable modes is seen in Figs. 2(b) and 2(c), where normalized perturbations of the potential energy, $\delta W(t)$, and $\text{sign}(\delta W)$ are shown, respectively [the values of the normalization coefficient are given

in the legend of Fig. 2(b)]. The quantity δW is calculated from Eqs. (3.6) and (2.30) of Ref. 39

$$\delta W = -\frac{1}{2} \int_{\text{box}} (\xi \cdot \mathbf{F}(\xi)) d\tau, \quad (15)$$

$$\mathbf{F}(\xi) = \nabla[\kappa p(\nabla \cdot \xi) + (\xi \cdot \nabla)p] + \mathbf{J} \times \delta \mathbf{B} - \mathbf{B} \times [\nabla \times \delta \mathbf{B}], \quad (16)$$

where $\mathbf{J} = [0, J_y, 0]$ is the background current density and $d\tau$ is the element of volume. Equation (16) does not contain the term depending on the electric potential ϕ because solution (1)–(6) ensures $\phi = 0$.

Expectedly, the plots of $\delta W(t)$ and $\text{sign}(\delta W)$ exhibit the concurrence of the stable ($\delta W > 0$) and unstable ($\delta W < 0$) modes at the early times and dominance of the latter at the later times. In a symmetrical CS (black curve), alternating-sign variations of δW are observed within one period ($T_0 = 196$) of the oscillating mode [Fig. 2(a)] and finishing yet after $t = 182$. For $\varphi = 7.5^\circ$, it happens at $t = 40$; for $\varphi = \{15^\circ, 60^\circ\}$, it happens at $t = 6$; and for $\varphi = 30^\circ$, δW is strictly negative, i.e., the solution is purely unstable. As a matter of interest, in the cumulative quantity δW , the dominance of the unstable mode begins much faster than in the single-point solution shown in Fig. 2(a). This means that the oscillating mode survives longer in the sheet center. At late times, the solutions for δU and δW demonstrate the same exponential growth, as it is seen from Table I, where growth rates, derived from these two solutions, are compared.

The dependence of the instability growth rate on the parameter φ is plotted in Fig. 3(a) for several values of the wavelength. It is seen that within the considered wavelength band, γ grows with the increasing tilt angle for any λ . The curves $\lambda = L$ and $\lambda = L/2$ are almost identical in accordance with the prediction of the DG model [see Fig. 3(b)]. Notably, in numerical simulations, the reduction of the wavelength is equivalent to an increase in the mesh step and hence the numerical dissipation, i.e., for a fixed mesh step, the accuracy goes down with decreasing λ . This is the reason why the value of $\gamma(\varphi = 60^\circ$ and $\lambda = L/2)$ is somewhat lower than $\gamma(60^\circ, L)$. According to Table I, for $\lambda = L$, the increment of instability grows approximately as $\varphi^{2/3}$.

In Fig. 3(b), numerically obtained dispersion curves $\gamma(k_y)$ are plotted for $\varphi = \{0^\circ, 7.5^\circ, 15^\circ, 30^\circ, 60^\circ\}$ by solid curves. The plot demonstrates that an increase in the tilt angle scales up the growth rate almost uniformly in a

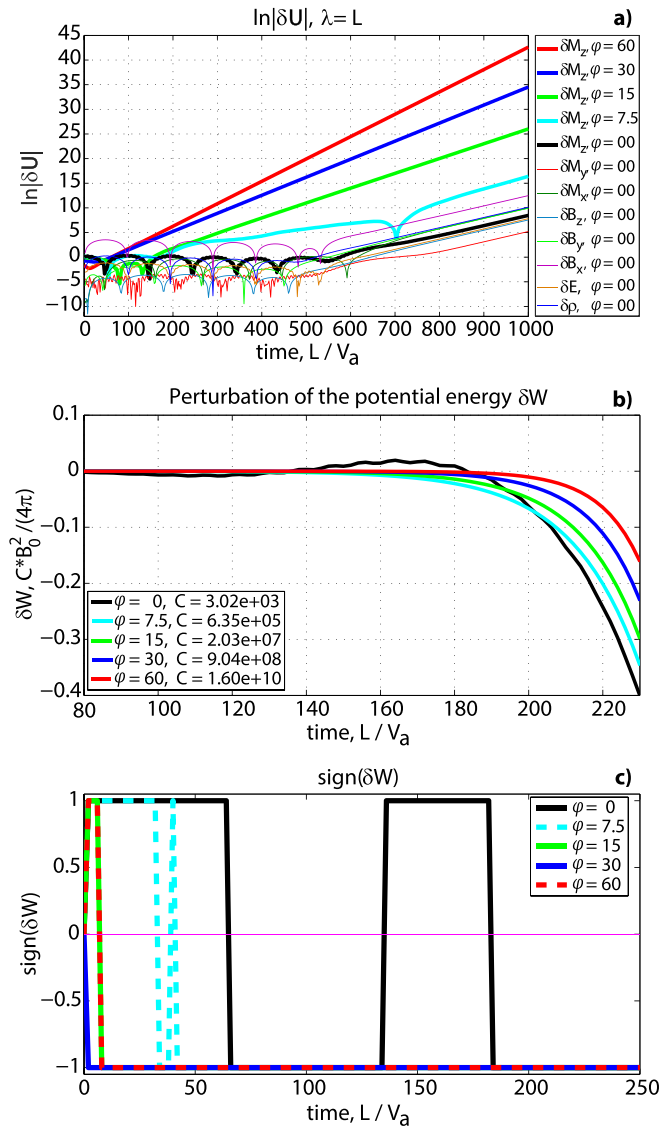


FIG. 2. Top: the solution of the system (9) in a symmetrical CS ($\varphi = 0^\circ$) for wavelength $\lambda = L$ in the point (15, 0) is shown as $\ln|\delta U|(t)$ by thin curves. Five thick curves plot the solutions for δM_z in the same point for $\varphi = \{0^\circ, 7.5^\circ, 15^\circ, 30^\circ, 60^\circ\}$. Middle: normalized perturbations of the potential energy δW , calculated from Eqs. (15) and (16) for $\varphi = \{0^\circ, 7.5^\circ, 15^\circ, 30^\circ, 60^\circ\}$. The values of the normalization coefficient C are given in the legend. Bottom: the sign of δW .

TABLE I. The growth rate γ of the unstable mode as a function of parameter φ for wavelength $\lambda = L$. First column: φ . Second column: mean value of $\Delta(\ln|\delta U|)/\Delta t \pm$ standard deviation. Third column: $(1/2)\Delta(\ln|\delta W|)/\Delta t$. The computational time interval is $\Delta t = [800, 1200]$.

φ (deg)	$\gamma (V_a/L)$	$\gamma (V_a/L)$
0	$0.02084 \pm 4 \times 10^{-5}$	0.02086
7.5	$0.0258 \pm 1 \times 10^{-4}$	0.02579
15	$0.03001 \pm 4 \times 10^{-5}$	0.03002
30	$0.036608 \pm 5 \times 10^{-6}$	0.03661
60	$0.04536 \pm 8 \times 10^{-5}$	0.04537

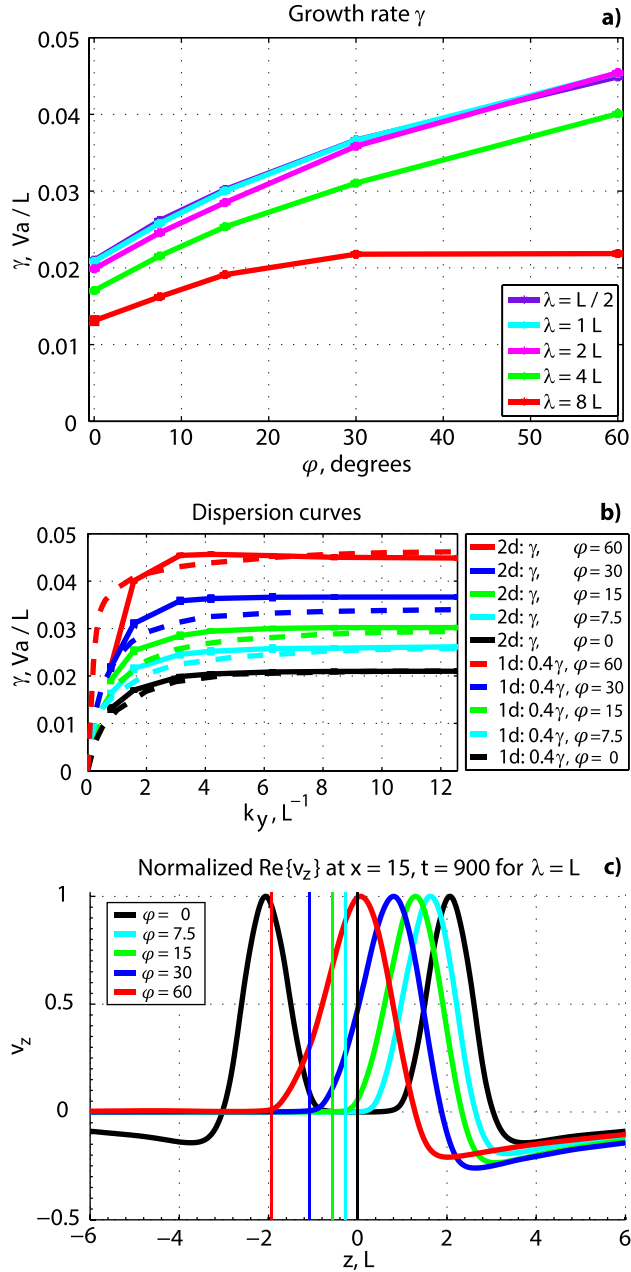


FIG. 3. Top: the growth rate (γ) of the unstable mode for different values of the wavelength (λ) is shown as a function of parameter φ . The values of λ are given in the legend. Middle: dispersion curves $\gamma(k_y)$ as obtained from 2D numerical simulations are shown by solid curves for $\varphi = 60^\circ$ (red), 30° (blue), 15° (green), 7.5° (cyan), and 0° (black). The curves $0.4\gamma(k_y)$, derived from the solution of the 1D spectral problem (11)–(14), are plotted by dashed curves of the same colors. Bottom: profiles of the normal velocity component perturbation $\text{Re}\{v_z(z)\}$ in a cross-section $x = 15$ at $t = 900$ for wavelength $\lambda = L$ are shown for $\varphi = 60^\circ$ (red), 30° (blue), 15° (green), 7.5° (cyan), and 0° (black). Vertical lines of the same colors mark the CS centers.

short-wavelength band $k_y > 4L^{-1}$. In the long-wavelength band, the effect weakens with decreasing k_y . The descending slope of the red solid curve in the range $k_y > 4L^{-1}$ is a numerical effect of a finite mesh step, as discussed above. Numerical solutions are compared to the solutions of the spectral problem (11)–(14), which are subdivided into two branches: oscillating and exponentially growing. Growth rates of the unstable branch, reduced 2.5 times, are plotted in

Fig. 3(b) by dashed curves. The figure shows that the accuracy of the 1D solution is better in the short-wavelength band. Here, analytical and numerical dispersion curves match qualitatively, although the 1D curve overestimates the growth rate ~ 2.5 times, almost uniformly on k_y and the tilt angle (the lowest scale factor of 2.3 is detected for $\varphi = 30^\circ$). In the long-wavelength band, the agreement of 1D and 2D solutions goes down with growing φ .

In Fig. 3(c), profiles of the normal velocity component perturbation $\text{Re}\{v_z(z)\}$ in the cross-section $x = 15$ at $t = 900$ for wavelength $\lambda = L$ are shown for $\varphi = \{0^\circ, 7.5^\circ, 15^\circ, 30^\circ, 60^\circ\}$. At such a late time, the solution is evolved to the set of well-developed eigenfunctions, and hence, the magnitude of v_z has no meaning; we normalize it to 1. The figure exhibits three features: (a) in bent sheets, the symmetry of the solution is lost; (b) the solution for $\varphi = 30^\circ$ possesses the largest asymmetrical part ($\max|v_z^{\text{even}}| = 0.52$, $\max|v_z^{\text{odd}}| = 0.49$); and (c) except for the strictly symmetrical case $\varphi = 0^\circ$, perturbations are localized in the upper part of the sheet, above the CS center.

VI. DISCUSSION AND CONCLUSIONS

We have examined the influence of the magnetotail current sheet bending in a vertical (x, z) plane on the sheet stability to the transversal mode $\sim \exp(ik_y y)$. 2.5D linear MHD equations are solved numerically for several equilibrium background configurations, differing from each other by the dipole tilt angle. For a benchmark, a symmetrical CS (zero tilt angle) is considered. It is found that in symmetrical CS, both stable and unstable regimes coexist. The growth rate of the unstable branch is rather small, the typical timescale amounts $1/\gamma \approx 50L/V_a$, and the period of the oscillating solution is $T_0 \approx 200L/V_a$. According to Fig. 2(a), these two branches interplay without visible domination of instability until $\sim 500L/V_a$. As it was found in Ref. 28, the Kan-like background model, used in the present study, is more suitable for thick current sheets. Assuming $L \sim 4\text{--}6 \times 10^3$ km and $V_a \sim 400$ km/s, the typical timescale L/V_a may be estimated as 10–15 s, and consequently, the domination of the unstable mode comes in sight after $\tau \sim 1.5\text{--}2$ h, which is rather long compared to the substorm timescale [making the same estimate by the behavior of $\text{sign}(\delta W)$, we derive a smaller value of $\tau \sim 30\text{--}45$ min]. With the growing tilt angle, γ increases and τ reduces; for the maximum possible value of φ , the growth rate becomes 2.25 times higher. Besides, when the tilt angle reaches some threshold value ($\sim 0.5 \varphi_{\text{max}}$ in our model), the oscillating branch of the solution vanishes and the CS becomes fully unstable. In such sheets, the typical timescale is defined by the growth rate only; therefore, it shortens an order of magnitude, $\tau = 1/\gamma \sim 5$ min.

Notably, the sheet destabilization is not caused by a local peak of the normal magnetic component or local depletion in the field line entropy, which is calculated as⁹

$$S(\mathbf{r}_c) = p \int_{\mathbf{r}_c}^{\mathbf{r}_b} \frac{ds}{B}, \quad (17)$$

where ds is the elementary increment of the magnetic field line length. All integration trajectories start at the current sheet center (\mathbf{r}_c) and end at the boundary (\mathbf{r}_b). The boundary is placed at $x=1$ to eliminate singularities. Both B_z and S demonstrate smooth monotonic profiles along the CS center: B_z decreases (not shown), and entropy increases tailward for any value of φ [see Fig. 4(a)]. Hence, the stability of the Kan-like CS to the transversal (flapping) mode is not governed by the usual entropy criterion.¹⁰

At the same time, the results of numerical simulations show qualitative agreement [Fig. 3(b)] with the double-gradient model.³⁰ Apart from the growth rates, profiles of the normal velocity component perturbation [Fig. 3(c)] show distinct correlation with the behavior of the function $U_0(z)$, defined by Eq. (12). In Fig. 4(b), profiles $U_0(z)$ are plotted in the cross-section $x=15$. In the symmetrical CS (black curve), U_0 exhibits two symmetric minima, located at $z \approx \pm 2$, very close to the maximums of $v_z(z)$ at Fig. 3(c). With increasing φ , the right minimum (upper part of the sheet) deepens and the left one (lower part) flattens. Note that the negative values of U_0 assume an unstable solution. Perturbations of v_z (and other quantities) are also confined in the upper “semiplane.”

In a planar equilibrium CS near to the sheet center, the function U_0 represents the main part of the second derivative of the total pressure, $\partial^2 \Pi / \partial z^2$, divided by ρ .²⁷ In Ref. 27, we have studied the same transversal mode in a simple symmetrical background configuration with a single-peaked function U_0 . It was found that in such configurations, the CS stability to the flapping mode is controlled by the sign of $\partial^2 \Pi / \partial z^2$ in the sheet center: the sheet is stable when this quantity is positive (Π has a minimum) and unstable in the opposite case. In the present case, the situation is more complicated. Profiles of the total pressure at $x=15$ are shown in Fig. 4(c). In a symmetrical sheet (black curve), $\Pi(z)$ has a tiny minimum at $z=0$ at the background of a (comparatively) huge global maximum. With the growing value of φ , the central minimum flattens, and for $\varphi \geq 30^\circ$, it disappears totally. Figure 4(d), showing the profiles of $\Pi' = \partial \Pi / \partial z$, provides a better visualization of this feature. It is seen that for $\varphi = \{0, 7.5, 15\}$ $\Pi'(z)$ crosses zero near (exactly in the symmetrical case) the sheet center. For higher values of the tilt angle, Π' stays negative there, i.e., the local minimum of total pressure is evanesced. This explains the coexistence of oscillating and unstable modes for small values of φ and vanishing of the first one in highly asymmetric sheets, as observed in Fig. 2.

The double-peaked profile of the total pressure brings an important modification of the solution as compared to single-peaked configurations. Even in a symmetrical sheet, the perturbation $v_z(z)$ has an alternating-sign profile (black curve in Fig. 3(c); compare to a strictly positive solution plotted in Fig. 5 of Ref. 33). Since the solution is harmonic in the y direction, this means a space-periodical stretching and compression of the sheet. For any non-zero tilt angle, perturbations in the lower part of the sheet disappear; in the upper part, stretching/compression enhances with growing φ , and the maximum velocity shear is reached for $\varphi = 30^\circ$.

Clearly, a CS compression should play in favor of magnetic reconnection.

Summing up, the symmetry breaking is confirmed to be a destabilizing factor for magnetotail dynamics, as it was

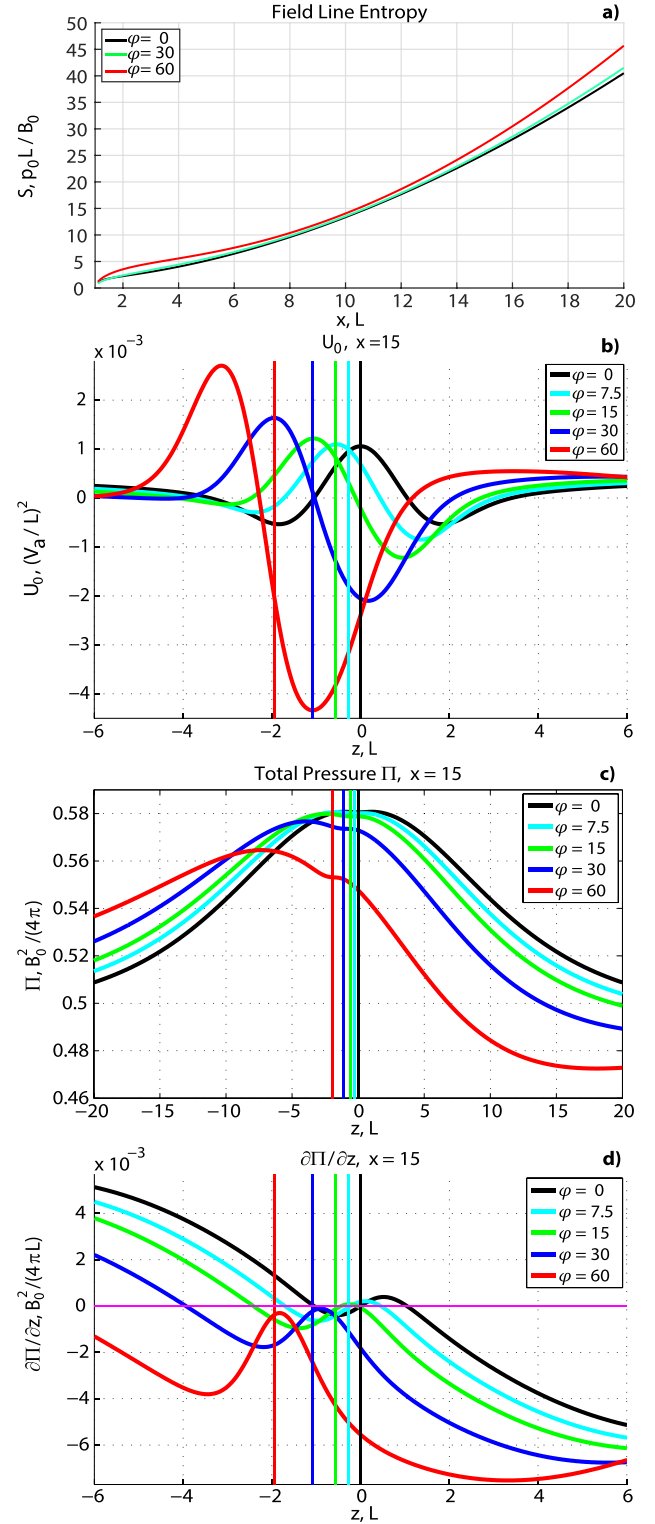


FIG. 4. Panel (a): the field line entropy, calculated from Eq. (17), is shown for $\varphi = 0^\circ$ (black), $\varphi = 30^\circ$ (green), and $\varphi = 60^\circ$ (red). Panels (b)–(d): profiles of the background specific functions at $x=15$ are shown for $\varphi = 60^\circ$ (red), 30° (blue), 15° (green), 7.5° (cyan), and 0° (black). The CS centers are plotted by vertical lines of the same colors. Panel (b): the function $U_0(z)$, calculated from Eq. (12). Panel (c): the total pressure $\Pi(z)$. Panel (d): the total pressure derivative $\partial \Pi / \partial z$.

first supposed by Kivelson and Hughes.¹ Our previous hypothesis, claiming that the stability of the magnetotail CS to the transversal mode may be controlled by the distribution of the total pressure, has got a further extension. It is found that a local minimum of Π in the sheet center allows flapping-like waves; bending of the sheet destroys this minimum and any corresponding harmonic solution, enhancing the unstable mode, ordered by a global maximum of Π . Figure 4(c) demonstrates that even very weak deviations of $\Pi(z)$ from constant are substantial for magnetotail dynamics. The smallness of the total pressure variations results in an extension of the typical timescale, but it does not mean that perturbation amplitudes are small. The space-periodical compression of the CS by flapping-like perturbations seems to be a possible mechanism for triggering magnetic reconnection.

Since present results are obtained in a simple linear MHD approximation, a number of important issues stayed out of scope. For example, a compression of the CS should bring forth kinetic effects, and the nonlinear properties of the unstable flapping mode are also in question. Hence, further development would require using more powerful tools such as fully 3D MHD and Particle-in-Cell simulations. It is also worth mentioning that the exact Kan-like solution, utilized in the present study, allows resolving very long-periodic CS oscillations, caused by very small ($\sim \epsilon^2$, where $\epsilon \sim L/L_x$ scales the CS stretching) variations of the background parameters. This significant advantage is materialized at the expense of a number of model limitations, such as isothermality and constant current velocity (see discussion in Ref. 28). For studies, focused on short-timescale processes, more realistic background configurations may be constructed by using approximate tail-like solutions, introduced in Refs. 40 and 41, where magnetic potential $\Psi = \Psi_0(x, z) + O(\epsilon^2)$. However, when flapping oscillations are under consideration, the accuracy of this approximation may appear insufficient.

ACKNOWLEDGMENTS

This study was supported by the Austrian Science Fund (FWF) (Nos. P 27012-N27 and I 3506-N27) and by the Russian Science Foundation (RSF) (Grant No. 18-47-05001). The authors thank Anna V. Egorova for her help with preparation of the images.

¹M. G. Kivelson and W. J. Hughes, "On the threshold for triggering substorms," *Planet. Space Sci.* **38**, 211–220 (1990).

²N. Partamies, T. Pulkkinen, R. McPherron, K. McWilliams, C. Bryant, E. Tanskanen, H. Singer, G. Reeves, and M. Thomsen, "Different magnetospheric modes: Solar wind driving and coupling efficiency," *Ann. Geophys.* **27**, 4281–4291 (2009).

³M. Kubyshkina, N. Tsyganenko, V. Semenov, D. Kubyshkina, N. Partamies, and E. Gordeev, "Further evidence for the role of magnetotail current shape in substorm initiation," *Earth, Planets Space* **67**, 139 (2015).

⁴M. Kubyshkina, V. Semenov, N. Erkaev, E. Gordeev, S. Dubyagin, N. Ganushkina, and M. Shukhtina, "Relations between v_z and B_x components in solar wind and their effect on substorm onset," *Geophys. Res. Lett.* **45**, 3760–3767, <https://doi.org/10.1002/2017GL076268> (2018).

⁵E. V. Panov, R. Nakamura, W. Baumjohann, M. G. Kubyshkina, A. V. Artemyev, V. A. Sergeev, A. A. Petrukovich, V. Angelopoulos, K.-H. Glassmeier, J. P. McFadden *et al.*, "Kinetic ballooning/interchange instability in a bent plasma sheet," *J. Geophys. Res.* **117**, A06228, <https://doi.org/10.1029/2011JA017496> (2012).

⁶L. Juusola, Y. Pfau-Kempf, U. Ganse, M. Battarbee, T. Brito, M. Grandin, L. Turc, and M. Palmroth, "A possible source mechanism for magnetotail current sheet flapping," *Ann. Geophys.* **36**, 1027–1035 (2018).

⁷M. I. Sitnov, V. G. Merkin, M. Swisdak, T. Motoba, N. Buzulukova, T. E. Moore, B. H. Mauk, and S. Ohtani, "Magnetic reconnection, buoyancy, and flapping motions in magnetotail explosions," *J. Geophys. Res.* **119**, 7151–7168, <https://doi.org/10.1002/2014JA020205> (2014).

⁸P. L. Pritchett and F. V. Coroniti, "Structure and consequences of the kinetic ballooning/interchange instability in the magnetotail," *J. Geophys. Res.* **118**, 146–159, <https://doi.org/10.1029/2012JA018143> (2013).

⁹J. Birn, V. Merkin, M. Sitnov, and A. Otto, "MHD stability of magnetotail configurations with a B_z hump," *J. Geophys. Res.: Space Phys.* **123**, 3477–3492, <https://doi.org/10.1029/2018JA025290> (2018).

¹⁰K. Schindler and J. Birn, "MHD stability of magnetotail equilibria including a background pressure," *J. Geophys. Res.* **109**, 10208, <https://doi.org/10.1029/2004JA010537> (2004).

¹¹N. F. Ness, "The Earth's magnetic tail," *J. Geophys. Res.* **70**, 2989–3005, <https://doi.org/10.1029/JZ070i013p02989> (1965).

¹²V. Sergeev, V. Angelopoulos, C. Carlson, and P. Sutcliffe, "Current sheet measurements within a flapping plasma sheet," *J. Geophys. Res.* **103**, 9177–9187, <https://doi.org/10.1029/97JA02093> (1998).

¹³T. L. Zhang, W. Baumjohann, R. Nakamura, A. Balogh, and K.-H. Glassmeier, "A wavy twisted neutral sheet observed by Cluster," *Geophys. Res. Lett.* **29**, 5-1–5-4, <https://doi.org/10.1029/2002GL015544> (2002).

¹⁴C. Shen, X. Li, M. Dunlop, Z. X. Liu, A. Balogh, D. N. Baker, M. Hapgood, and X. Wang, "Analyses on the geometrical structure of magnetic field in the current sheet based on cluster measurements," *J. Geophys. Res.* **108**, 1168, <https://doi.org/10.1029/2002JA009612> (2003).

¹⁵A. Runov, V. A. Sergeev, W. Baumjohann, R. Nakamura, S. Apatenkov, Y. Asano, M. Volwerk, Z. Vörös, T. L. Zhang, A. Petrukovich *et al.*, "Electric current and magnetic field geometry in flapping magnetotail current sheets," *Ann. Geophys.* **23**, 1391–1403 (2005).

¹⁶A. A. Petrukovich, W. Baumjohann, R. Nakamura, A. Runov, A. Balogh, and C. Carr, "Oscillatory magnetic flux tube slippage in the plasma sheet," *Ann. Geophys.* **24**, 1695–1704 (2006).

¹⁷C. Forsyth, M. Lester, R. C. Fear, E. Lucek, I. Dandouras, A. N. Fazakerley, H. Singer, and T. K. Yeoman, "Solar wind and substorm excitation of the wavy current sheet," *Ann. Geophys.* **27**, 2457–2474 (2009).

¹⁸Z. Rong, C. Shen, A. Petrukovich, W. Wan, and Z. Liu, "The analytic properties of the flapping current sheets in the earth magnetotail," *Planet. Space Sci.* **58**, 1215–1229 (2010).

¹⁹G. Wang, M. Volwerk, R. Nakamura, P. Boakes, T. Zhang, A. Yoshikawa, and D. Baishev, "Flapping current sheet with superposed waves seen in space and on the ground," *J. Geophys. Res.: Space Phys.* **119**, 10078, <https://doi.org/10.1002/2014JA020526> (2014).

²⁰D. J. McComas, H. E. Spence, C. T. Russell, and M. A. Saunders, "The average magnetic field draping and consistent plasma properties of the Venus magnetotail," *J. Geophys. Res.: Space Phys.* **91**, 7939–7953, <https://doi.org/10.1029/JA091iA07p07939> (1986).

²¹E. Dubinin, M. Fraenz, J. Woch, T. Zhang, J. Wei, A. Fedorov, S. Barabash, and R. Lundin, "Bursty escape fluxes in plasma sheets of Mars and Venus," *Geophys. Res. Lett.* **39**, L01104, <https://doi.org/10.1029/2011GL049883> (2012).

²²Z. Rong, S. Barabash, G. Stenberg, Y. Futaana, T. Zhang, W. Wan, Y. Wei, X. Wang, L. Chai, and J. Zhong, "The flapping motion of the venusian magnetotail: Venus express observations," *J. Geophys. Res.: Space Phys.* **120**, 5593–5602, <https://doi.org/10.1002/2015JA021317> (2015).

²³B. H. Mauk, D. C. Hamilton, T. W. Hill, G. B. Hospodarsky, R. E. Johnson, C. Parancas, E. Roussos, C. T. Russell, D. E. Shemansky, E. C. Sittler *et al.*, "Fundamental plasma processes in Saturn's magnetosphere," in *Saturn from Cassini-Huygens*, edited by M. K. Dougherty, L. W. Esposito, and S. M. Krimigis (Springer, 2009), pp. 281–331.

²⁴F. Bagenal and P. A. Delamere, "Flow of mass and energy in the magnetospheres of Jupiter and Saturn," *J. Geophys. Res.: Space Phys.* **116**, A05209, <https://doi.org/10.1029/2010JA016294> (2011).

²⁵M. Volwerk, N. André, C. S. Arridge, C. M. Jackman, X. Jia, S. E. Milan, A. Radioti, M. F. Vogt, A. P. Walsh, R. Nakamura *et al.*, "Comparative magnetotail flapping: An overview of selected events at Earth, Jupiter and Saturn," *Ann. Geophys.* **31**, 817–833 (2013).

²⁶D. B. Korovinskiy, A. Divin, N. V. Erkaev, V. V. Ivanova, I. B. Ivanov, V. S. Semenov, G. Lapenta, S. Markidis, H. K. Biernat, and M. Zellinger, "MHD modeling of the double-gradient (kink) magnetic instability," *J. Geophys. Res.* **118**, 1146–1158, <https://doi.org/10.1002/jgra.50206> (2013).

- ²⁷D. Korovinskiy, N. Erkaev, V. Semenov, I. Ivanov, S. Kiehas, and I. Ryzhkov, "On the influence of the local maxima of total pressure on the current sheet stability to the kink-like (flapping) mode," *Phys. Plasmas* **25**, 022904 (2018).
- ²⁸D. B. Korovinskiy, D. I. Kubyshkina, V. S. Semenov, M. V. Kubyshkina, N. V. Erkaev, and S. A. Kiehas, "On application of asymmetric Kan-like exact equilibria to the Earth magnetotail modeling," *Ann. Geophys.* **36**, 641–653 (2018).
- ²⁹N. A. Tsyanenko, "Modeling the Earth's magnetospheric magnetic field confined within a realistic magnetopause," *J. Geophys. Res.: Space Phys.* **100**, 5599–5612, <https://doi.org/10.1029/94JA03193> (1995).
- ³⁰N. V. Erkaev, V. S. Semenov, I. V. Kubyshkin, M. V. Kubyshkina, and H. K. Biernat, "MHD model of the flapping motions in the magnetotail current sheet," *J. Geophys. Res.* **114**, A03206, <https://doi.org/10.1029/2008JA013728> (2009).
- ³¹P. H. Yoon and A. T. Y. Lui, "A class of exact two-dimensional kinetic current sheet equilibria," *J. Geophys. Res.: Space Phys.* **110**, A01202, <https://doi.org/10.1029/2003JA010308> (2005).
- ³²V. Semenov, D. Kubyshkina, M. Kubyshkina, I. Kubyshkin, and N. Partamies, "On the correlation between the fast solar wind flow changes and substorm occurrence," *Geophys. Res. Lett.* **42**, 5117–5124, <https://doi.org/10.1002/2015GL064806> (2015).
- ³³D. Korovinskiy, I. Ivanov, V. Semenov, N. Erkaev, and S. Kiehas, "Numerical linearized MHD model of flapping oscillations," *Phys. Plasmas* **23**, 062905 (2016).
- ³⁴A. G. Kulikovskii, N. V. Pogorelov, and A. Y. Semenov, *Mathematical Aspects of Numerical Solution of Hyperbolic Systems* (CRC Press, 2000).
- ³⁵A. Kurganov, S. Noelle, and G. Petrova, "Semidiscrete central-upwind schemes for hyperbolic conservation laws and Hamilton–Jacobi equations," *SIAM J. Sci. Comput.* **23**, 707–740 (2001).
- ³⁶S. Gottlieb, C.-W. Shu, and E. Tadmor, "Strong stability-preserving high-order time discretization methods," *SIAM Rev.* **43**, 89–112 (2001).
- ³⁷G. Tóth, "The $\nabla \cdot \mathbf{B} = 0$ constraint in shock-capturing magnetohydrodynamics codes," *J. Comput. Phys.* **161**, 605–652 (2000).
- ³⁸N. V. Erkaev, V. S. Semenov, and H. K. Biernat, "Magnetic double-gradient instability and flapping waves in a current sheet," *Phys. Rev. Lett.* **99**, 235003 (2007).
- ³⁹I. B. Bernstein, E. Frieman, M. Kruskal, and R. Kulsrud, "An energy principle for hydromagnetic stability problems," *Proc. R. Soc. London A* **244**, 17–40 (1958).
- ⁴⁰K. Schindler, "A self-consistent theory of the tail of the magnetosphere," in *Earth's Magnetospheric Processes*, edited by B. M. McComas (D. Reidel, Dordrecht, Holland, 1972), Vol. 32, pp. 200–209.
- ⁴¹J. Birn, R. Sommer, and K. Schindler, "Open and closed magnetospheric tail configurations and their stability," *Astrophys. Space Sci.* **35**, 389–402 (1975).